Nano Research
2021, 14(5): 1273–1279

ISSN 1998-0124 CN 11-5974/O4
https://doi.org/10.1007/s12274-020-3102-4

Research Article

Multilevel structured carbon film as cathode host for Li-S batteries with superhigh-areal-capacity

Bin He, Wen-Cui Li, Zhi-Yuan Chen, Lei Shi, Yu Zhang, Ji-Li Xia, and An-Hui Lu (✉)

State Key Laboratory of Fine Chemicals, School of Chemical Engineering, Dalian University of Technology, Dalian 116024, China

Received: 4 August 2020 / **Revised:** 7 September 2020 / **Accepted:** 8 September 2020

ABSTRACT

The commercialization of lithium-sulfur (Li-S) battery could be accelerated by designing advanced sulfur cathode with high sulfur utilization and stable cycle life at a high sulfur loading. To allow the energy density of Li-S batteries comparable to that of commercial Li-ion batteries, the areal capacity of sulfur cathode should be above 4 mA·h·cm^{-2}. In general, a high sulfur loading often causes rapid capacity fading by slowing electron/ion transport kinetics, catastrophic shuttle effect and even cracking the electrodes. To address this issue, herein, a multilevel structured carbon film is built by covering highly conductive CNTs and hollow carbon nanofiber together with carbon layer via chemical vapor deposition. The self-standing carbon film exhibits well-interweaved conductive network, hollow fibrous structure and abundant N, O co-doped active sites, which combine the merits of high electronic conductivity (1,200 S·m^{-1}), high porosity and polar characteristic in one host. Benefiting from this attractive multilevel structure, the obtained sulfur cathode based on the carbon film host shows an ultra-high areal capacity of 8.9 mA·h·cm^{-2} at 0.2 C with outstanding cyclability over 60 cycles. This work shed light on designing advanced sulfur host for Li-S batteries with high areal capacity and high cycle stability, and might make a contribution to the commercialization of Li-S batteries.

KEYWORDS

multilevel structure, carbon film, sulfur host, conductivity, areal capacity

1 Introduction

Lithium-sulfur (Li-S) batteries have been emerging as one of the most promising energy storage systems due to their ultrahigh theoretical energy density, cost effectiveness, and environmental compatibility compared with conventional lithium-ion batteries (LIBs) [1–4]. However, the commercialization of Li-S batteries is still hindered by several technical issues, including low active material utilization, poor cycling life, and low coulombic efficiencies, owing to the insulating nature of sulfur and the dissolution of intermediate lithium polysulfides (LiPS) into the organic electrolyte [5–8]. In the past decades, much efforts have been expended to solve these problems by utilizing novel host materials [9–11], constructing LiPS blocking interlayers [12–14], developing new electrolytes [15, 16] and applying functional binders [17, 18]. Regarding the fabrication of sulfur electrode with a sulfur loading of < 2.0 mg·cm^{-2}, Li-S batteries can so far exhibit high sulfur utilization and long cycle life [19–21]. Nevertheless, one of the remained practical issues is that the low sulfur loading in the sulfur cathode reduces the mass ratio of active materials to inactive materials (e.g., current collectors, binders, additives, electrolyte and packaging). As a consequence, the fabricated cells have considerably low energy density, thus less competitive capability [22].

To allow the energy density of Li-S batteries comparable to that of commercial Li-ion batteries, the areal capacity of sulfur cathode should be above 4 mA·h·cm^{-2}. It means that high sulfur loadings (≥ 4 mg·cm^{-2}) together with high sulfur utilization (≥ 60%) are essential for a sulfur cathode [23]. Nevertheless, efforts to simultaneously improve the sulfur loadings and the utilization degree of sulfur are quite challenging, since these two factors are in contradiction [24]. As the sulfur loading increasing, the electrode becomes thicker, resulting in ultra-long transport pathway and high resistance for the diffusion of Li-ions. Consequently, the kinetics of both Li-ions and electrons were limited, thus dramatically lowering the utilization degree of sulfur [25]. Moreover, thick electrodes usually suffer from cracking due to the significant volume expansion of sulfur during charge/discharge process, worsening the cycle stability of Li-S batteries [26]. Another critical issue for the high sulfur loading cathode is that large amounts of LiPS dissolution are generated, leading to a much worse cycle stability [27]. These dissolved LiPS may additionally convert to solid sulfur species (S_8, Li_2S, and Li_2S_2) and precipitate on the electrode/electrolyte interfaces, blocking the Li-ion transportation channels.

Recently, researchers have demonstrated that the synthesis of three-dimensional (3D) materials as sulfur hosts by constructing 3D interlinked electron and ion channels within the electrode could promote the intimate electrolyte/electrode contact and the high-rate charge transfer, being preferable for improving sulfur utilization at high sulfur loadings [28–31]. For example, Ren and co-workers reported 3D graphene foam/reduced graphene oxide as sulfur host, such integrated electrode exhibited fast ion and electron transportation, delivering a high areal capacity of 10.3 mA·h·cm^{-2} at 0.2 C [32]. Hu developed a 3D aligned porous carbon matrix by using carbonized wood with reduced graphene oxide (RGO) filled inside the micro-channels for high sulfur mass loading. In this cathode, RGO

Address correspondence to anhuilu@dlut.edu.cn

serves as an electronically conductive network to enhance the electron transport, and the low-tortuosity and open microchannels can allow better electrolyte permeation. Consequently, the fabricated sulfur electrodes with a sulfur loading of 7.8 mg·cm^{-2} showed a high areal capacity of 6.7 mA·h·cm^{-2} [33]. However, only relying on physical confinement and weak chemisorption by these host materials was not sufficient to suppress diffusion of the polar LiPS over a long lifespan, especially for the high-loading cell design. Therefore, we are still on the way to look for new structured sulfur cathode that possess high sulfur loading, high sulfur utilization, and good cycle stability without sacrificing the areal energy density.

In this study, we prepared a multilevel structured carbon film consisting of well-interweaved carbon nanotubes (CNTs) and hollow carbon nanofibers (HCFs). They were chemically "welded" together using a conformal carbon coating layer with high graphitization degree via chemical vapor deposition (CVD). This multilevel structured carbon film exhibits an exceptionally high conductivity of 1,200 S·m^{-1}, hollow structure for encapsulation of sulfur and oxygen and nitrogen co-doped active sites strongly binding LiPS. Such designed carbon film was directly used as a working electrode for sulfur electrodeposition via electrolysis approach. The sulfur loading can be tuned from 4.7 to 10.2 mg·cm^{-2} by varying the electrolysis time and the thickness of the electrode. As a result, the cathode with sulfur loading as high as 10.2 mg·cm^{-2} retains a high areal capacity of 8.9 mA·h·cm^{-2} after 60 cycles. Our results indicate that the rational design of carbon host with multilevel structure indeed makes it possible to fabricate high performance sulfur cathode even with a very high sulfur loading.

2 Experimental

2.1 Chemicals

All chemicals were used as received without any further purification. $MnSO_4·H_2O$, $KClO_3$, CH_3COOK, CH_3COOH, and sulfur were purchased from Sinopharm Chemical Reagent Co. Ltd. CNTs were purchased from Chengdu Organic Chemicals Co. Ltd.. Deionized water was used in all experiments.

2.2 Synthesis of multilevel structured CNT/HCF thin film

The CNT/HCF carbon film is prepared via templating and chemical vapor deposition method. MnO_2 nanowires with lengths larger than 50 μm (Fig. S1(a) in the Electronic Supplementary Material (ESM)) synthesized according to previous literature [34] were selected as the starting template. Subsequently, the ultralong MnO_2 nanowires and CNTs (length: < 10 μm, outer diameter: 30–80 nm, electric conductivity: > 10,000 S·m^{-1}) with a ratio of 17:1 were dispersed in water and stirred for 2 h to form stable dispersion. The dispersion was filtered by vacuum filtration with common filter paper, washed several times with distilled water and absolute ethanol, respectively, and dried at 60 °C for 12 h. Then, the self-standing CNT/MnO_2 hybrid thin film can be prepared (Fig. S1(a) in the ESM). The content of CNTs in the CNT/MnO_2 film is ~ 5.5 wt.%. The CNTs and MnO_2 nanowires are interwoven together to form abundant macropores (Fig. S1(b) in the ESM), allowing easy diffusion of carbon source molecules for CVD. Then, the carbon layers were coated on the MnO_2 nanowires through CVD method at 800 °C for 1 h, by using aniline as carbon source to yield the CNT/MnO@C thin film. During the CVD process, MnO_2 was reduced to MnO, confirmed by the XRD analysis in Fig. S2 in the ESM. After carbon coating, the sample CNT/MnO@C is well maintained self-standing structure (Fig. S3(a) in the ESM) with pod-like nanowires interwoven together (Fig. S3(b) in the ESM), which offers enough interconnected and continuous macropores. Moreover, the pod-like nanowires are chemically "welded" together (Fig. S3(c) in the ESM). The MnO_2 nanowires were reduce by carbon source during the CVD process, in which the MnO_2 nanowires will shrink to form MnO particles, meanwhile, these MnO particles are wrapped by carbon layers. As a result, the peapod-like architecture is observed. The TEM images in Figs. S3(d)–S3(f) in the ESM show that the carbon layers act as a welding reagent to chemically connect the pod-like nanowires together. Subsequently, the obtained black thin film CNT/MnO@C was immersed in 6 M HCl aqueous solution to remove the MnO nanofibers templates, and then washed with deionized water to obtain the CNT/HCF hybrid thin film. Before carbon coating, the weight of CNT in CNT/MnO_2 is ~ 0.0066 g. After CVD and removing the templates, the weight of CNT/HCF film is ~ 0.045 g. Thus, the content of CNTs in the CNT/HCF film is ~ 15 wt.%. The control sample HCF was prepared with the same procedures without adding CNTs.

2.3 Synthesis of CNT/HCF-S cathode

Sulfur was incorporated into the self-standing CNT/HCF via the electrolysis approach according to our previous work [10]. Typically, electrolysis was carried out in a two-electrode system, with the CNT/HCF as the working electrode. The working solution was 300 ml 0.15 M Na_2S aqueous solution, containing 1.016 g KH_2PO_4 and 1.060 g Na_2HPO_4 as well as 300 mg sulfur. The sulfur-carbon composite obtained was washed by distilled water and dried at 50 °C for 24 h and was denoted CNT/HCF-S. The electrodes CNT/HCF-S-1, CNT/HCF-S-2, and CNT/HCF-S-3 were prepared with sulfur loadings of around 4.7, 7.3, and 10.2 mg·cm^{-2}, respectively by changing the electrodeposition time and the thickness of the CNT/HCF film. The weight of the electrode CNT/HCF-S-1 is ~ 9 mg·cm^{-2} and the thickness of the electrodes CNT/HCF-S-1 is ~ 0.22 mm.

Commercial carbon nanofiber paper (Toray; c-CF) treated with concentrated nitric acid for 2 h was used as a working electrode for sulfur electrodeposition using the same method to prepare c-CF-S cathode. HCF film was directly used as a working electrode for sulfur electrodeposition to prepare HCF-S cathode. The sulfur loading in the c-CF-S and HCF-S is about 4.0 and 4.3 mg·cm^{-2}, respectively. The thickness of the electrodes c-CF-S and HCF-S is about 0.19 and 0.2 mm, respectively.

2.4 Characterization methods

The sample morphology was investigated by field-emission scanning electron microscopy (SEM) using a Hitachi S-4800 instrument at 10 kV. Nitrogen adsorption isotherm was measured at 77 K with an ASAP 3000 adsorption analyzer (Micromeritics). Before the measurements, the sample CNT/HCF was degassed under vacuum at 200 °C for 4 h and CNT/HCF-S-1 was degassed under vacuum at 50 °C for 12 h until the pressure was less than 5 Pa. The Brunauer–Emmett–Teller (BET) method was used to calculate the specific surface areas (S_{BET}). Total pore volumes were calculated from the amount adsorbed at a relative pressure, P/P_0 of 0.99. X-ray diffraction (XRD) patterns were obtained with a Rigaku D/MAX-2400 diffractometer using Cu Kα radiation (40 kV, 100 mA, λ = 1.54056 Å). Transmission electron microscopy (TEM) analyses were carried out with a Tecnai G220S-Twin instrument operating at 200 kV. Samples for TEM analysis was prepared by dropping an ethanol droplet of the products on carbon-coated copper grids and drying at room temperature. Thermogravimetric (TG) analysis was

measured from 40 to 800 °C with a heating rate of 10 °C·min^{-1} under an air flow, using a STA449 F3 Jupiter thermogravimetric analyzer (NETZSCH). X-ray photoelectron spectroscopy (XPS) data were obtained with a PHI 5000 Versaprobe spectrometer equipped with an Al Kα X-ray source. The conductivity of CNT/HCF was tested by four-tip probes method. The Raman spectrum of CNT/HCF was collected on a homemade DL-2 microscopic Raman spectrometer, using the 532 nm line of a KIMMON laser.

2.5 Electrochemical tests

CR2025 coin cells were assembled to evaluate the electrochemical performance of the electrode materials using the CNT/HCF-S thin film directly as cathode material, lithium metal as an anode, and Celgard 2400 as a separator. 1.0 M LiTFSI in dimethoxyethane (DME)/1,3-dioxolane (DOL) (1:1, by volume) and 0.02 M Li_2S_6 containing 2 wt.% $LiNO_3$ was used as the electrolyte. The electrolyte addition with the electrolyte/sulfur (E/S) ratio of ~ 15:1. The electrolyte amount is 55 μl for CNT/HCF-S-1. The thickness and the diameter of the Li foil is ~ 1 and ~ 15.6 mm, respectively. The current and capacities were calculated based on the mass of element sulfur. Discharge/charge measurements were conducted at a voltage interval of 1.7 to 2.8 V using a Land CT2001A (LAND, Wuhan China) battery test system. Cyclic voltammetry (CV) measurements were performed on CHI660D electrochemical work station at a scan rate of 0.05 mV·s^{-1} after activation at 0.1 C for three cycles. Electrochemical impedance spectroscopy (EIS) measurements were carried out in the frequency range 100 kHz to 0.01 Hz on CHI660D.

3 Results and discussion

The CNT/HCF carbon film is prepared via templating and chemical vapor deposition method, as schematically illustrated in Fig. 1(a) (for experimental details see the experimental section). The fabricated multilevel structured CNT/HCF carbon film shows the well-retained self-standing architecture (Fig. 1(b)), which is essentially a copy of the morphology of the CNT/MnO@C thin film (Fig. S3(a) in the ESM). The SEM image in Fig. 1(c) shows that the CNT/HCF film consists of interwoven pod-like carbon nanofibers and CNTs. Such structure creates abundant macropores in the carbon framework, allowing easy diffusion of electrolyte. The lengths of the carbon nanofibers are generally larger than 50 μm (Fig. S4(a) in the ESM), which are beneficial to the long-range charge transfer [29]. Moreover, the pod-like carbon nanofibers interwove together (Fig. 1(d)) to build the robust and highly conductive carbon skeleton.

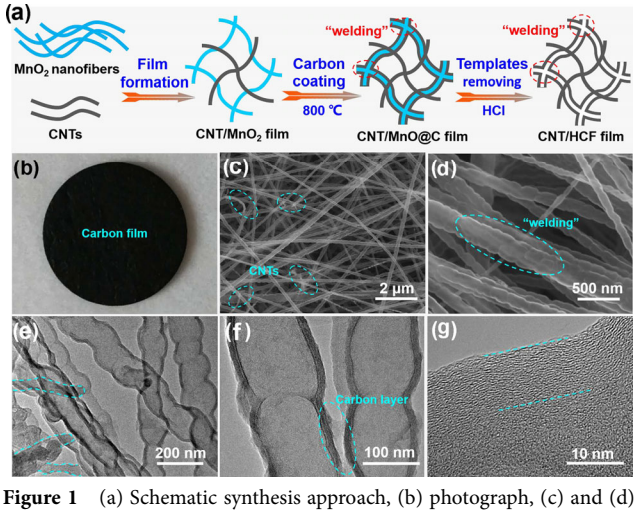

Figure 1 (a) Schematic synthesis approach, (b) photograph, (c) and (d) SEM images and (e)–(g) TEM images of CNT/HCF carbon film.

The TEM images (Figs. 1(e)–1(g)) show that the pod-like carbon nanofibers contain hollow spaces, generating sufficient internal cavities larger than 50 nm for accommodating a high sulfur loading. The thickness of the carbon shell is estimated to be about 10 nm. The TEM image in Fig. 1(f) shows that the carbon layers act as a welding reagent to chemically connect the HCFs together, which is consistent with the SEM observation in Fig. 1(d). It is noted that the welded HCFs can improve electrical conductivity by reduce the contact resistance. Additionally, the HCFs are partially graphitized (Fig. 1(g)), which can further enhance the conductivity of the CNT/HCF carbon film. The Raman spectrum of CNT/HCF in Fig. S5 in the ESM shows two intense bands located at 1,357 and 1,587 cm^{-1}, assigned to the D and G bands of carbon materials, respectively. The intensity ratio of the D-band to the G-band (I_D/I_G) is 0.97, suggesting that the carbon component in CNT/HCF is semi-crystalline. The peak at ~ 2,900 cm^{-1} is called D+G bands, which correspond to the second-order of Raman spectrum in combination modes [9]. The determined conductivity of CNT/HCF is 1,200 S·m^{-1}, which is an order of magnitude higher than those of carbon black such as Vulcan XC-72 carbon (150 S·m^{-1}) [35].

The XRD pattern of CNT/HCF is depicted in Fig. S2 in the ESM. The diffraction peak of the carbon element is observed at 25.6°. Several weak diffraction peaks corresponding to MnO in the XRD pattern of CNT/HCF indicated that most of the MnO templates were removed by acid treatment. Abundant cavities and only a few particles were observed in the CNT/HCF thin film (Fig. S4(b) in the ESM), further supporting that most of the MnO templates were removed. TG analysis reveals that the residual MnO content in the CNT/HCF is ~ 30 wt.%, as shown in Fig. S6 in the ESM. The textural properties of the CNT/HCF were assessed by nitrogen sorption isotherm, as shown in Fig. S7 in the ESM. The specific surface area and total pore volume of the CNT/HCF film were evaluated to be 68 m^2·g^{-1} and 0.16 cm^3·g^{-1}, respectively. On the basis of the above mentioned results, the self-standing carbon film exhibits multilevel structure with well-interweaved conductive network and hollow fibrous structure, which combines the merits of high electronic conductivity (1,200 S·m^{-1}), sufficient internal cavities to confine sulfur species, and continuous open channels to facilitate fast electrolyte ion transportation in one host. These advantages can simultaneously meet the demands of a sulfur host material for Li-S batteries with high areal capacity and long cycle lives.

The CNT/HCF carbon film is self-standing, with a continuous conductive carbon framework, an open pore system and good mechanical strength, allowing it act as a working electrode directly for sulfur electrodeposition. The corresponding sulfur electrodes (CNT/HCF-S) were prepared via an electrolysis approach according to our previous report [10]. For comparative study, the electrodes CNT/HCF-S-1, CNT/HCF-S-2, and CNT/HCF-S-3 were prepared with sulfur loadings of around 4.7, 7.3, and 10.2 mg·cm^{-2}, respectively.

For the representative structure analysis, we take CNT/HCF-S-1 as one sample. As seen in Fig. S8 in the ESM, the sulfur exists in a crystalline state (JCPDS No. 08-0247) with typical sharp diffraction peaks, which confirms that sulfur is incorporated into CNT/HCF by an electrolysis approach. The SEM image of cross section in Fig. S9(a) in the ESM shows that CNT/HCF-S-1 exhibits layer-by-layer stacking structure. As seen in Fig. 2(a), the CNT/HCF-S-1 shows abundant open channels constructed by interweaved HCFs, favoring the

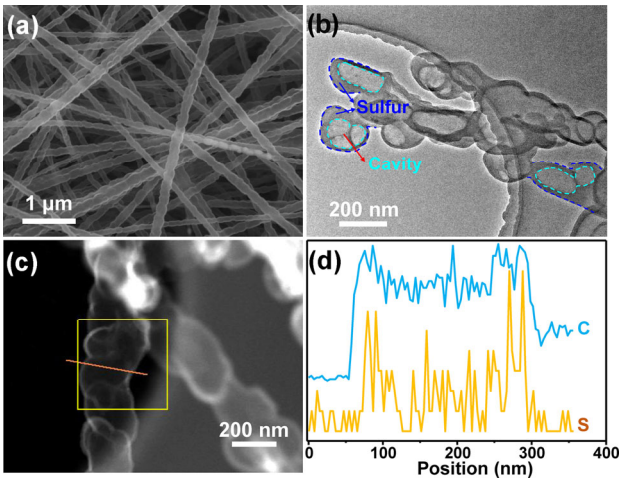

Figure 2 (a) SEM image and (b)–(d) STEM images and linear EDX element distributions of CNT/HCF-S-1.

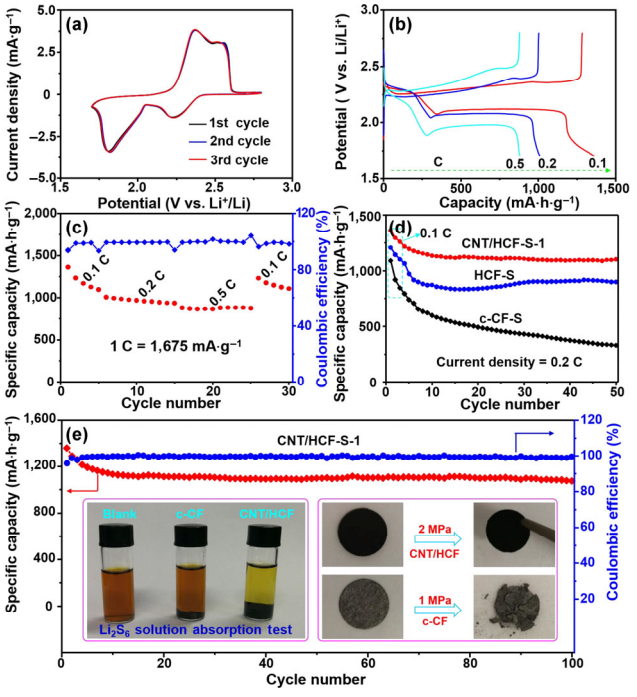

Figure 3 (a) Cyclic voltammetry measured between 1.7 and 2.8 V. (b) Discharge/charge voltage profiles at various rates from 0.1 to 0.5 C. (c) Discharge/charge capacity cycled at various rates from 0.1 to 0.5 C. (d) Capacity retention of material cycled at 0.2 C, in comparison with HCF-S and c-CF-S material. (e) Long-term cyclability and Coulombic efficiency of CNT/HCF-S-1 at 0.2 C. The insets are static adsorption test of CNT/HCF and c-CF with Li_2S_6 solution, and the photographs of CNT/HCF and c-CF films before and after subjected to vertical pressures.

penetration of the electrolyte for the high-sulfur-loading electrodes. Moreover, no sulfur particles are visible in the composite in Fig. 2(a) and Figs. S9(b) and S9(c) in the ESM. TEM observation (Fig. 2(b)) shows that sulfur is incorporated into the cavities of the carbon nanofibers and attached to the carbon inner wall. The EDX linear scan across one CNT/HCF fiber demonstrates that there is a high content of S around the carbon wall (Figs. 2(c) and 2(d)), further proving that sulfur is attached to the carbon wall. Nitrogen sorption isotherms of CNT/HCF-S-1 in Fig. S7 in the ESM show that it has almost no specific surface area and no pore volume after sulfur incorporation. The elemental mappings of CNT/HCF-S-1 (Fig. S10 in the ESM) show that sulfur and carbon are distributed uniformly in the hybrid film. These results are consistent with our previous report [10], in which the electrodeposition method can ensure the sulfur highly dispersed and electrically connected to the carbon host in nature, leading to improved sulfur utilization.

A CV test was conducted to evaluate the electrochemical performance of the CNT/HCF-S-1 electrode (Fig. 3(a)). During the discharge process, the reduction peaks at the cathodic scans of 2.23 and 1.82 V present a typical two-step reduction of sulfur into high-order LiPS and Li_2S/Li_2S_2, respectively. While in the anodic scan, the oxidation peaks at 2.37 and 2.53 V correspond to the transformation of Li_2S into high-order LiPS and eventually to elemental sulfur, respectively [36, 37]. In subsequent scans, the overlapping cathodic and anodic peaks maintain their shape and display no obvious intensity changes and potential shifts, suggesting superior cyclic stability and highly reversible redox reactions. It is noted that the CV curves is a bit distorted from the regular shape, which is mainly caused by overpotential, especially under high sulfur loading conditions [38, 39].

The galvanostatic charge-discharge curves of the CNT/HCF-S-1 (Fig. 3(b)) display a typical two-plateau behavior of Li-S battery, which are consistent with the results of CV. Moreover, the CNT/HCF-S-1 electrode delivers a high initial discharge capacity of 1,362 $mA·h·g^{-1}$, corresponding to specific areal capacity of 6.4 $mA·h·g^{-1}$ and 81.5% of the theoretical capacity of sulfur (1,675 $mA·h·g^{-1}$), indicating a high sulfur utilization. The gravimetric and volumetric energy densities are ~ 1,500 $Wh·kg^{-1}$ and ~ 610 $Wh·l^{-1}$ for CNT/HCF-S-1 cathode at 0.1 C based on the discharge voltage of 2.1 V. Next, the CNT/HCF-S-1 electrode was subjected to cycle at various current densities from 0.1 to 0.5 C for evaluating the rate capability. As shown in Fig. 3(c), the discharge capacities decrease gradually with increasing current density and stabilize at around 939 and 876 $mA·h·g^{-1}$ when cycled at 0.2 and 0.5 C, respectively. When the current density was returned to 0.1 C after cycling at different rates, the specific capacity recovered to 1,232 $mA·h·g^{-1}$, indicating the good stability of the CNT/HCF-S-1 during testing at various rates.

Figure 3(d) shows the cycling performances of CNT/HCF-S-1, HCF-S, and c-CF-S. The electrodes are discharged at 0.1 C for three cycles to activate the electrode and facilitate the wetting of the electrolyte. After activation, the CNT/HCF-S-1 cathode at 0.2 C shows a relatively good cyclic stability of 1,101 $mA·h·g^{-1}$ after 50 cycles. Similarly, the cycling performance of HCF-S cathode at 0.2 C shows a good cyclic stability but relatively low specific capacity of 899 $mA·h·g^{-1}$ after 50 cycles due to its low conductivity. In contrast, the control sample c-CF-S shows a relatively poor cyclic stability of 329 $mA·h·g^{-1}$ after 50 cycles. As demonstrated in Fig. 3(e), CNT/HCF-S-1 cathode showed a high capacity of 1,077 $mA·h·g^{-1}$ after 100 cycles at 0.2 C and a stabilized Coulombic efficiency over 98.5%. Such good electrochemical performance of the CNT/HCF-S-1 electrode could be attributed to the multilevel structure of the highly conductive carbon film and highly dispersed sulfur that benefits the redox reaction and confinement of sulfur. These results are further supported by the electrochemical impedance spectroscopy measurements in Fig. S11 in the ESM. The CNTs/HCNF-S-1 shows the lowest charge-transfer resistance compared with HCF-S and c-CF-S, which is very conducive to the electrochemical performance.

Additionally, the CNT/HCF can trap the LiPS effectively to inhibit the shuttle reaction and avoid the mass loss of the active materials, which is confirmed by the LiPS adsorption measurements (the inset in Fig. 3(e)). The Li_2S_6 solution mixed with CNT/HCF carbon film shows much obvious discoloration than that mixed with c-CF, indicating that CNT/HCF can

effectively trap LiPS in the Li-S battery. To figure out the high adsorptivity of CNT/HCF toward LiPS, XPS analyses are further carried out. The survey spectrum in Fig. 4(a) shows a C 1s peak (≈ 284.6 eV), a N 1s peak (≈ 399.0 eV), and an O 1s peak (≈ 531.5 eV). The relative atomic contents of C, N, and O are calculated to be around 83.24%, 8.22%, and 8.54%, respectively. The O element introduced into the CNT/HCF can improve the affinity and binding strength of LiPS to the carbon film [40]. Besides, the N 1s spectrum is fitted into three typical peaks at the binding energy of 398.3, 400.3, and 402.0 eV (Fig. 4(b)), consistent with pyridinic, pyrrolic, and graphitic nitrogen, respectively [41]. Among these nitrogen heteroatoms, the pyrrolic-N and pyridinic-N have lone pair electron and high electronegativity, which can adsorb positive charged Li^+ in LiPS by forming $LiS_nLi^+\cdots N$ binding, thereby resulting in an effective trapping of LiPS [42].

The CNT/HCF film exhibits robust mechanical properties by against the compressive strength up to 2.0 MPa (the inset in Fig. 3(e)), therefore it can tolerate the volumetric expansion of sulfur during the discharge process. Moreover, the SEM images (Figs. 5(a) and 5(b)) of CNT/HCF-S-1 after 50 cycles show that CNT/HCF-S-1 retain the original, fibrous, and interconnected morphology, indicating the good structural stability of the cathode. The cross-sectional SEM observations of CNT/HCF-S-1 after 50 cycles in Figs. S9(d) and S9(e) in the ESM show that the electrode becomes denser due to the battery packing pressure. Moreover, some sulfur species attached to the HCFs (Figs. 5(a) and 5(b) and Figs. S9(e) and S9(f) in the ESM), indicating that the active material was kept inside the carbon film. The SEM elemental maps of CNT/HCF-S-1 after 50 cycles (Figs. 5(d)–5(h)) show that sulfur is still uniformly loaded in the carbon film without obvious sulfur-rich area. These results indicate the excellent structure stability of the electrode and the strong interaction between LiPS with the carbon film.

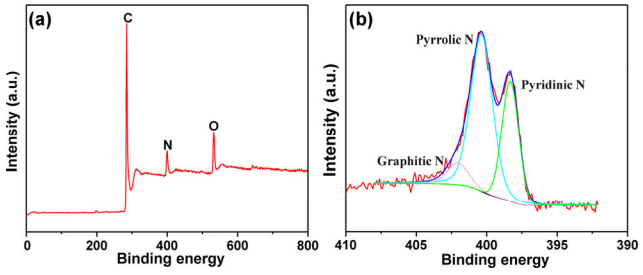

Figure 4 (a) X–ray photoelectron spectrum, (b) X–ray photoelectron spectrum of N1s for the sample CNT/HCF.

For practical applications of an electrode, a high sulfur loading is necessary in order to obtain a high overall areal capacity of sulfur cathodes. We further evaluated the performances of the electrodes CNT/HCF-S-2 and CNT/HCF-S-3 with high loading of about 7.3 and 10.2 mg·cm^{-2}, respectively, and the results are shown in Fig. 5(i). The CNT/HCF-S-2 and CNT/HCF-S-3 deliver high initial discharge capacity of 1,260 and 1,130 mA·h·g^{-1} at 0.1 C, respectively, corresponding to specific areal capacities of 9.2 and 11.5 mA·h·cm^{-2}. After 30 cycles, the CNT/HCF-S-2 and CNT/HCF-S-3 show high capacity retention with areal capacities of 7.0 and 9.1 mA·h·cm^{-2} at 0.2 C, respectively (Fig. 5(j)). These results are superior to that of commercial Li-ion batteries. After 60 cycles, the CNT/HCF-S-2 and CNT/HCF-S-3 still show high capacity retention with corresponding areal capacity of 6.9 and 8.9 mA·h·cm^{-2} at 0.2 C, indicating a high cyclic stability of these two electrodes. The specific capacity and areal capacity value are at a rather high level in comparison to the recent publications showing a sulfur loading higher than 3.5 mg·cm^{-2} as summarized in Fig. 5(k) [24, 29, 43–54]. The great capability for sulfur loading and satisfactory sulfur electrochemistry of the CNT/HCF-S electrode can be ascribed to the following factors: (i) The ultralong and chemically welded HCFs with high degree of graphitization offer significant long-range, high conductivity and low contact

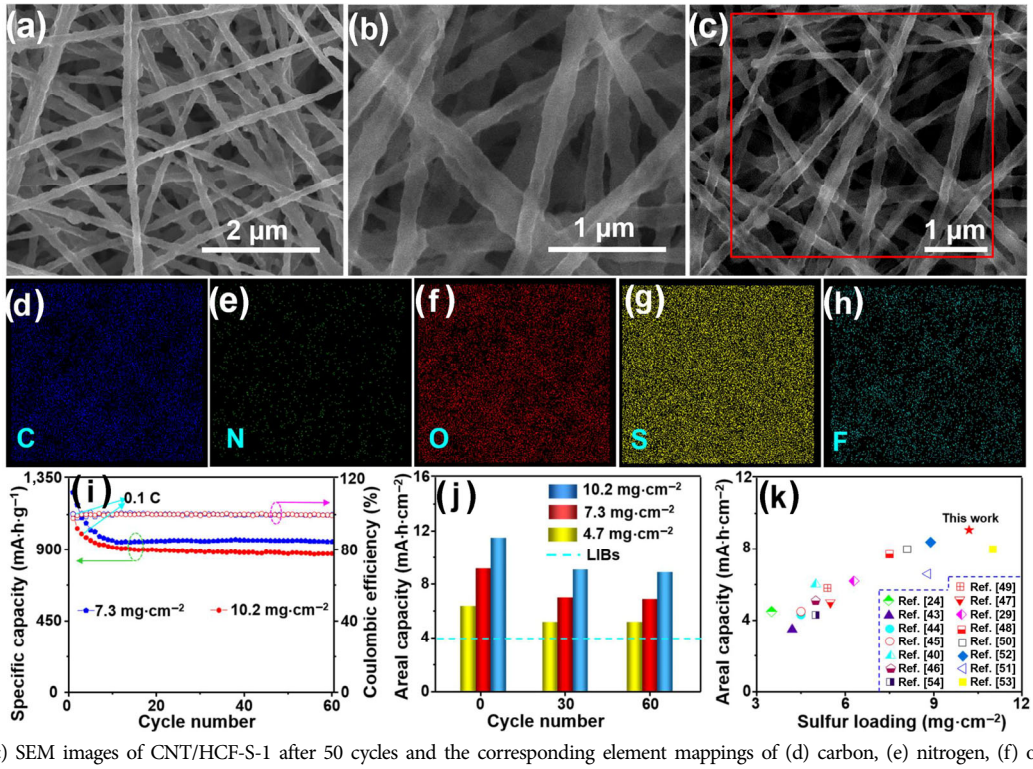

Figure 5 (a)–(c) SEM images of CNT/HCF-S-1 after 50 cycles and the corresponding element mappings of (d) carbon, (e) nitrogen, (f) oxygen, (g) sulfur, (h) fluorine. (i) Cycling performance of the cathode CNT/HCF-S-2 and CNT/HCF-S-3. (j) Areal capacities of the three electrodes with different sulfur loadings at different cycles. (k) Comparison of areal capacity of this work with that of Li-S batteries from recent publications in which the sulfur loadings is higher than 3.5 mg·cm^{-2}.

resistance. (ii) CNTs contribute great conductivity and weave the HCFs into a self-standing electrode, devoid of polymer binders, further improves the conductivity of the cathode. (iii) The intertwined CNTs and HCFs not only offer enough interconnected and continuous open channels to facilitate fast electrolyte ion transportation but also build the robust and highly conductive skeleton to ensure the electrode integrity during the charge/discharge process. (iv) The N/O dual-doped porous HCFs with sufficient internal cavities larger than 50 nm ensure a uniform sulfur distribution, strong sulfur confinement and high LiPS adsorption capability, and abundant electrode/electrolyte interfaces for reaction of LiPS and precipitation of S_8/Li_2S/Li_2S_2.

4 Conclusions

In this study, we prepared a multilevel structured carbon film through chemically welded N/O dual-doped, ultralong hollow carbon nanofibers with CNTs together as the self-standing sulfur host for Li-S batteries. The carbon film with robust and highly conductive skeleton, hollow fibrous structure, and interconnected and continuous open channels is particularly intriguing to the high sulfur loading. At the same time, oxygen and nitrogen doped carbon matrix enables physically and chemically affinity to sulfur and lithium sulfide species. Attributed to these merits, outstanding cyclability with an ultra-low capacity decay of 0.115% per cycle over 100 cycles and an ultra-high specific areal capacity of 6.4 mA·h·cm^{-2} were achieved for the electrode with sulfur loading of 4.7 mg·cm^{-2}. Even with a sulfur loading as high as 10.2 mg·cm^{-2}, the cathode can deliver an ultra-high areal capacity of 11.5 mA·h·cm^{-2} at 0.1 C. This work presents a simple but effective welded steel frame-inspired strategy to develop multilevel structured sulfur host for Li-S batteries, which can also be applied in many other energy storage and conversion applications.

Acknowledgements

This work was supported by the National Natural Science Foundation of China (Nos. 21776041 and 21875028), and Cheung Kong Scholars Programme of China (No. T2015036).

Electronic Supplementary Material: Supplementary material (SEM images of the CNT/MnO_2; X-ray diffraction patterns of CNT/MnO@C and CNT/HCF; SEM images and TEM image of CNT/MnO@C; SEM image, TEM image, Raman spectrum and TGA curves of CNT/HCF; SEM image of CNT/HCF-S-1, etc.) is available in the online version of this article at https://doi.org/10.1007/s12274-020-3102-4.

References

[1] Ye, C.; Jiao, Y.; Jin, H. Y.; Slattery, A. D.; Davey, K.; Wang, H. H.; Qiao, S. Z. 2D MoN-VN heterostructure to regulate polysulfides for highly efficient lithium-sulfur batteries. *Angew. Chem., Int. Ed.* **2018**, *57*, 16703–16707.

[2] Qian, J.; Wang, F. J.; Li, Y.; Wang, S.; Zhao, Y. Y.; Li, W. L.; Xing, Y.; Deng, L.; Sun, Q.; Li, L. et al. Electrocatalytic interlayer with fast lithium-polysulfides diffusion for lithium-sulfur batteries to enhance electrochemical kinetics under lean electrolyte conditions. *Adv. Funct. Mater.* **2020**, *30*, 2000742.

[3] Kim, J.; Elabd, A.; Chung, S. Y.; Coskun, A.; Choi, J. W. Covalent triazine frameworks incorporating charged polypyrrole channels for high-performance lithium-sulfur batteries. *Chem. Mater.* **2020**, *32*, 4185–4193.

[4] Zhang, J.; Huang, H.; Bae, J.; Chung, S. H.; Zhang, W. K.; Manthiram, A.; Yu, G. H. Nanostructured host materials for trapping sulfur in rechargeable Li-S batteries: Structure design and interfacial chemistry. *Small Methods* **2018**, *2*, 1700279.

[5] Wang, H. Q.; Zhang, W. C.; Xu, J. Z.; Guo, Z. P. Advances in polar materials for lithium-sulfur batteries. *Adv. Funct. Mater.* **2018**, *28*, 1707520.

[6] Yin, Y. X.; Xin, S.; Guo, Y. G.; Wan, L. J. Lithium-sulfur batteries: Electrochemistry, materials, and prospects. *Angew. Chem., Int. Ed.* **2013**, *52*, 13186–13200.

[7] Zhang, B.; Luo, C.; Deng, Y. Q.; Huang, Z. J.; Zhou, G. M.; Lv, W.; He, Y. B.; Wan, Y.; Kang, F. Y.; Yang, Q. H. Optimized catalytic WS_2-WO_3 heterostructure design for accelerated polysulfide conversion in lithium-sulfur batteries. *Adv. Energy Mater*, **2020**, *10*, 2000091.

[8] Chen, T.; Zhang, Z. W.; Cheng, B. R.; Chen, R. P.; Hu, Y.; Ma, L. B.; Zhu, G. Y.; Liu, J.; Jin, Z. Self-templated formation of interlaced carbon nanotubes threaded hollow Co_3S_4 nanoboxes for high-rate and heat-resistant lithium-sulfur batteries. *J. Am. Chem. Soc.* **2017**, *139*, 12710–12715.

[9] He, B.; Li, W. C.; Zhang, Y.; Yu, X. F.; Zhang, B. S.; Li, F.; Lu, A. H. Paragenesis BN/CNTs hybrid as a monoclinic sulfur host for high rate and ultra-long life lithium-sulfur battery. *J. Mater. Chem. A* **2018**, *6*, 24194–24200.

[10] He, B.; Li, W. C.; Yang, C.; Wang, S. Q.; Lu, A. H. Incorporating sulfur inside the pores of carbons for advanced lithium-sulfur batteries: An electrolysis approach. *ACS Nano* **2016**, *10*, 1633–1639.

[11] Wang, Z. S.; Shen, J. D.; Liu, J.; Xu, X. J.; Liu, Z. B.; Hu, R. Z.; Yang, L. C.; Feng, Y. Z.; Liu, J.; Shi, Z. C. et al. Self-supported and flexible sulfur cathode enabled via synergistic confinement for high-energy-density lithium-sulfur batteries. *Adv. Mater.* **2019**, *31*, 1902228.

[12] Ghazi, Z. A.; He, X.; Khattak, A. M.; Khan, N. A.; Liang, B.; Iqbal, A.; Wang, J. X.; Sin, H.; Li, L. S.; Tang, Z. Y. MoS_2/Celgard separator as efficient polysulfide barrier for long-life lithium-sulfur batteries. *Adv. Mater.* **2017**, *29*, 1606817.

[13] Li, Y. J.; Zhou, P.; Li, H.; Gao, T. T.; Zhou, L.; Zhang, Y. L.; Xiao, N.; Xia, Z. Z.; Wang, L.; Zhang, Q. H. et al. A freestanding flexible single-atom cobalt-based multifunctional interlayer toward reversible and durable lithium-sulfur batteries. *Small Methods* **2020**, *4*, 1900701.

[14] Wu, F.; Ye, Y. S.; Chen, R. J.; Qian, J.; Zhao, T.; Li, L.; Li, W. H. Systematic effect for an ultralong cycle lithium-sulfur battery. *Nano Lett.* **2015**, *15*, 7431–7439.

[15] Gao, J.; Sun, C. S.; Xu, L.; Chen, J.; Wang, C.; Guo, D. C.; Chen, H. Lithiated Nafion as polymer electrolyte for solid-state lithium sulfur batteries using carbon-sulfur composite cathode. *J. Power Sources* **2018**, *382*, 179–189.

[16] Li, X.; Wang, D. H.; Wang, H. C.; Yan, H. F.; Gong, Z. L.; Yang, Y. Poly(ethylene oxide)-$Li_{10}S_nP_2S_{12}$ composite polymer electrolyte enables high-performance all-solid-state lithium sulfur battery. *ACS Appl. Mater. Interfaces* **2019**, *11*, 22745–22753.

[17] Liu, J.; Zhang, Q.; Sun, Y. K. Recent progress of advanced binders for Li-S batteries. *J. Power Sources* **2018**, *396*, 19–32.

[18] Han, P.; Chung, S. H.; Chang, C. H.; Manthiram, A. Bifunctional binder with nucleophilic lithium polysulfide immobilization ability for high-loading, high-thickness cathodes in lithium-sulfur batteries. *ACS Appl. Mater. Interfaces* **2019**, *11*, 17393–17399.

[19] Jiang, G. S.; Xu, F.; Yang, S. H.; Wu, J. P.; Wei, B. Q.; Wang, H. Q. Mesoporous, conductive molybdenum nitride as efficient sulfur hosts for high-performance lithium-sulfur batteries. *J. Power Sources* **2018**, *395*, 77–84.

[20] Lu, Q.; Zhong, Y. J.; Zhou, W.; Liao, K. M.; Shao, Z. P. Dodecylamine-induced synthesis of a nitrogen-doped carbon comb for advanced lithium-sulfur battery cathodes. *Adv. Mater. Interfaces* **2018**, *5*, 1701659.

[21] Hao, B. Y.; Li, H.; Lv, W.; Zhang, Y. B.; Niu, S. Z.; Qi, Q.; Xiao, S. J.; Li, J.; Kang, F. Y.; Yang, Q. H. Reviving catalytic activity of nitrides by the doping of the inert surface layer to promote polysulfide conversion in lithium-sulfur batteries. *Nano Energy* **2019**, *60*, 305–311.

[22] Peng, H. J.; Huang, J. Q.; Cheng, X. B.; Zhang, Q. Review on high-loading and high-energy lithium-sulfur batteries. *Adv. Energy Mater.* **2017**, *7*, 1700260.

[23] Fang, R. P.; Zhao, S. Y.; Hou, P. X.; Cheng, M.; Wang, S. G.; Cheng, H. M.; Liu, C.; Li, F. 3D interconnected electrode materials with

ultrahigh areal sulfur loading for Li-S batteries. *Adv. Mater.* **2016**, *28*, 3374–3382.

[24] Lv, D. P.; Zheng, J. M.; Li, Q. Y.; Xie, X.; Ferrara, S.; Nie, Z. M.; Mehdi, L. B.; Browning, N. D.; Zhang, J. G.; Graff, G. L. et al. High energy density lithium-sulfur batteries: Challenges of thick sulfur cathodes. *Adv. Energy Mater.* **2015**, *5*, 1402290.

[25] Yang, X. F.; Chen, Y. Q.; Wang, M. R.; Zhang, H. Z.; Li, X. F.; Zhang, H. M. Phase inversion: A universal method to create high-performance porous electrodes for nanoparticle-based energy storage devices. *Adv. Funct. Mater.* **2016**, *26*, 8427–8434.

[26] Ding, N.; Chien, S. W.; Hor, T. S. A.; Liu, Z. L.; Zong, Y. Key parameters in design of lithium sulfur batteries. *J. Power Sources* **2014**, *269*, 111–116.

[27] Ai, G.; Dai, Y. L.; Mao, W. F.; Zhao, H.; Fu, Y. B.; Song, X. Y.; En, Y. F.; Battaglia, V. S.; Srinivasan, V.; Liu, G. Biomimetic ant-nest electrode structures for high sulfur ratio lithium-sulfur batteries. *Nano Lett.* **2016**, *16*, 5365–5372.

[28] Wu, X. W.; Xie, H.; Deng, Q.; Wang, H. X.; Sheng, H.; Yin, Y. X.; Zhou, W. X.; Li, R. L.; Guo, Y. G. Three-dimensional carbon nanotubes forest/carbon cloth as an efficient electrode for lithium-polysulfide batteries. *ACS Appl. Mater. Interfaces* **2017**, *9*, 1553–1561.

[29] Yuan, Z.; Peng, H. J.; Huang, J. Q.; Liu, X. Y.; Wang, D. W.; Cheng, X. B.; Zhang, Q. Hierarchical free-standing carbon-nanotube paper electrodes with ultrahigh sulfur-loading for lithium-sulfur batteries. *Adv. Funct. Mater.* **2014** *24*, 6105–6112.

[30] Ma, L. B.; Zhu, G. Y.; Zhang, W. J.; Zhao, P. Y.; Hu, Y.; Wang, Y. R.; Wang, L.; Chen, R. P.; Chen, T.; Tie, Z. X. et al. Three-dimensional spongy framework as superlyophilic, strongly absorbing, and electrocatalytic polysulfide reservoir layer for high-rate and long-cycling lithium-sulfur batteries. *Nano Res.* **2018**, *11*, 6436–6446.

[31] Ma, L. B.; Lin, H. N.; Zhang, W. J.; Zhao, P. Y.; Zhu, G. Y.; Hu, Y.; Chen, R. P.; Tie, Z. X.; Liu, J.; Jin, Z. Nitrogen-doped carbon nanotube forests planted on cobalt nanoflowers as polysulfide mediator for ultralow self-discharge and high areal-capacity lithium-sulfur batteries. *Nano Lett.* **2018**, *18*, 7949–7954.

[32] Hu, G. J.; Xu, C.; Sun, Z. H.; Wang, S. G.; Cheng, H. M.; Li, F.; Ren, W. C. 3D Graphene-foam-reduced-graphene-oxide hybrid nested hierarchical networks for high-performance Li-S batteries. *Adv. Mater.* **2016**, *28*, 1603–1609.

[33] Li, Y. J.; Fu, K. K.; Chen, C. J.; Luo, W.; Gao, T. T.; Xu, S. M.; Dai, J. Q.; Pastel, G.; Wang, Y. B.; Liu, B. Y. et al. Enabling high-areal-capacity lithium-sulfur batteries: designing anisotropic and low-tortuosity porous architectures. *ACS Nano* **2017**, *11*, 4801–4807.

[34] Lan, B.; Yu, L.; Lin, T.; Cheng, G.; Sun, M.; Ye, F.; Sun, Q. F.; He, J. Multifunctional free-standing membrane from the self-assembly of ultralong MnO_2 nanowires. *ACS Appl. Mater. Interfaces* **2013**, *5*, 7458–7464.

[35] Cui, Z. M.; Zu, C. X.; Zhou, W. D.; Manthiram, A.; Goodenough, J. B. Mesoporous titanium nitride -enabled highly stable lithium-sulfur batteries. *Adv. Mater.* **2016**, *28*, 6926–6931.

[36] Lin, C.; Qu, L. B.; Li, J. T.; Cai, Z. Y.; Liu, H. Y.; He, P.; Xu, X.; Mai, L. Q. Porous nitrogen-doped carbon/MnO coaxial nanotubes as an efficient sulfur host for lithium sulfur batteries. *Nano Res.* **2019**, *12*, 205–210.

[37] Hao, Z. X.; Zeng, R.; Yuan, L. X.; Bing, Q. M.; Liu, J. Y.; Xiang, J. W.; Huang, Y. H. Perovskite $La_{0.6}Sr_{0.4}CoO_{3-\delta}$ as a new polysulfide immobilizer for high-energy lithium-sulfur batteries. *Nano Energy* **2017**, *40*, 360–368.

[38] Li, Z.; Zhang, F.; Tang, L. B.; Tao, Y. Y.; Chen, H.; Pu, X. M.; Xu, Q. J.; Liu, H. M.; Wang, Y. G.; Xia, Y. Y. High areal loading and long-life cycle stability of lithium-sulfur batteries achieved by a dual-function ZnS-modified separator. *Chem. Eng. J.* **2020**, *390*, 124653.

[39] Hu, Y.; Chen, W.; Lei, T. Y.; Jiao, Y.; Wang, H. B.; Wang, X. P.; Rao, G. F.; Wang, X. F.; Chen, B.; Xiong, J. Graphene quantum dots as the nucleation sites and interfacial regulator to suppress lithium dendrites for high-loading lithium-sulfur battery. *Nano Energy* **2020**, *68*, 104373.

[40] Song, J. X.; Gordin, M. L.; Xu, T.; Chen, S. R.; Yu, Z. X.; Sohn, H.; Lu, J.; Ren, Y.; Duan, Y. H.; Wang, D. H. Strong lithium polysulfide chemisorption on electroactive sites of nitrogen-doped carbon composites for high-performance lithium-sulfur battery cathodes. *Angew. Chem., Int. Ed.* **2015**, *54*, 4325–4329.

[41] Liu, Z. X.; Li, J.; Xiang, J. W.; Cheng, S.; Wu, H.; Zhang, N.; Yuan, L. X.; Zhang, W. F.; Xie, J.; Huang, Y. H. et al. Hierarchical nitrogen-doped porous graphene/reduced fluorographene/sulfur hybrids for high-performance lithium-sulfur batteries. *Phys. Chem. Chem. Phys.* **2017**, *19*, 2567–2573.

[42] Chen, D.; Yang, R.; Chen, L. P.; Zou, Y. M.; Ren, B.; Li, L.; Li, S. C.; Yan, Y. L.; Xu, Y. H. One-pot fabrication of nitrogen and sulfur dual-doped graphene/sulfur cathode via microwave assisted method for long cycle-life lithium-sulfur batteries. *J. Alloys Compd.* **2018**, *746*, 116–124.

[43] Zhao, Q.; Zhu, Q. Z.; Miao, J. W.; Guan, Z. R. X.; Liu, H.; Chen, R. J.; An, Y. B.; Wu, F.; Xu, B. Three dimensional carbon current collector promises small sulfur molecule cathode with high areal loading for lithium-sulfur batteries. *ACS Appl. Mater. Interfaces* **2018**, *10*, 10882–10889.

[44] Pang, Q.; Kundu, D.; Nazar, L. F. A graphene-like metallic cathode host for long-life and high-loading lithium-sulfur batteries. *Mater. Horiz.* **2016**, *3*, 130–136.

[45] Zhou, W. D.; Guo, B. K.; Gao, H. C.; Goodenough, J. B. Low-cost higher loading of a sulfur cathode. *Adv. Energy Mater.* **2016**, *6*, 1502059.

[46] Zhu, X. Y.; Zhao, W.; Song, Y. Z.; Li, Q. C.; Ding, F.; Sun, J. Y.; Zhang, L.; Liu, Z. F. *In situ* assembly of 2D conductive vanadium disulfide with graphene as a high-sulfur-loading host for lithium-sulfur batteries. *Adv. Energy Mater.* **2018**, *8*, 1800201.

[47] Liang, X.; Rangom, Y.; Kwok, C. Y.; Pang, Q.; Nazar, L. F. Interwoven MXene Nanosheet/Carbon-nanotube composites as Li-S cathode hosts. *Adv. Mater.* **2017**, *29*, 1603040.

[48] Li, Y. J.; Fan, J. M.; Zhang, J. H.; Yang, J. F.; Yuan, R. M.; Chang, J.; Zheng, M. S.; Dong, Q. F. A honeycomb-like Co@N-C composite for ultrahigh sulfur loading Li-S batteries. *ACS Nano* **2017**, *11*, 11417–11424.

[49] Ma, L. B.; Yuan, H.; Zhang, W. J.; Zhu, G. Y.; Wang, Y. R.; Hu, Y.; Zhao, P. Y.; Chen, R. P.; Chen, T.; Liu, J. et al. Porous-shell vanadium nitride nanobubbles with ultrahigh areal sulfur loading for high-capacity and long-life lithium-sulfur batteries. *Nano Lett.* **2017**, *17*, 7839–7846.

[50] Yu, M. P.; Ma, J. S.; Xie, M.; Song, H. Q.; Tian, F. Y.; Xu, S. S.; Zhou, Y.; Li, B.; Wu, D.; Qiu, H. et al. Freestanding and sandwich-structured electrode material with high areal mass loading for long-life lithium-sulfur batteries. *Adv. Energy Mater.* **2017**, *7*, 1602347.

[51] Xiang, M. W.; Yang, L.; Zheng, Y. F.; Huang, J.; Jing, P.; Wu, H.; Zhang, Y.; Liu, H. A freestanding and flexible nitrogen-doped carbon foam/sulfur cathode composited with reduced graphene oxide for high sulfur loading lithium-sulfur batteries. *J. Mater. Chem. A* **2017**, *5*, 18020–18028.

[52] Ye, Y. S.; Wu, F.; Liu, Y. T.; Zhao, T.; Qian, J.; Xing, Y.; Li, W. L.; Huang, J. Q.; Li, L.; Huang, Q. M. et al. Toward practical high-energy batteries: A modular-assembled oval-like carbon microstructure for thick sulfur electrodes. *Adv. Mater.* **2017**, *29*, 1700598.

[53] Chen, X.; Yuan, L. X.; Hao, Z. X.; Liu, X. X.; Xiang, J. W.; Zhang, Z. R.; Huang, Y. H.; Xie, J. Free-standing Mn_3O_4@CNF/S paper cathodes with high sulfur loading for lithium-sulfur batteries. *ACS Appl. Mater. Interfaces* **2018**, *10*, 13406–13412.

[54] Pang, Q.; Nazar, L. F. Long-life and high-areal-capacity Li-S batteries enabled by a light-weight polar host with intrinsic polysulfide adsorption. *ACS Nano* **2016**, *10*, 4111–4118.